In Situ Failure Detection of Electronic Control Units Using Piezoresistive Stress Sensor

Prisacaru, Alexandru; Palczynska, Alicja; Theissler, Andreas; Gromala, Przemyslaw; Han, Bongtae; Zhang, Guo Qi

DOI
10.1109/TCPMT.2018.2816259

Publication date
2018

Document Version
Accepted author manuscript

Published in
IEEE Transactions on Components, Packaging and Manufacturing Technology

Citation (APA)
Prisacaru, A., Palczynska, A., Theissler, A., Gromala, P., Han, B., & Zhang, G. Q. (2018). In Situ Failure Detection of Electronic Control Units Using Piezoresistive Stress Sensor. *IEEE Transactions on Components, Packaging and Manufacturing Technology*, *8*(5), 750-763. https://doi.org/10.1109/TCPMT.2018.2816259

In-situ Failure Detection of Electronic Control Units Using Piezoresistive Stress Sensor

Alexandru Prisacaru, Alicja Palczynska, Andreas Theissler, Przemyslaw Gromala, *Member, IEEE*, Bongtae Han, Guo Qi Zhang, *Life Fellow, IEEE*

***Abstract*—Recent advancements in automotive technologies, most notably autonomous driving, demand electronic systems much more complex than realized in the past. The automotive industry has been forced to adopt advanced consumer electronics to satisfy the demand, and thus it becomes more challenging to assess system reliability while adopting the new technologies. The system level reliability can be enforced by implementing a process called condition monitoring. In this paper, a piezoresistive silicon based stress sensor is implemented to detect physical damages in outer molded electronic control units (ECU) subjected to reliability testing conditions. The test vehicle consists of six DPAK power packages and three stress sensors mounted on a Printed Circuit Board (PCB). A unique algorithm is proposed and implemented to handle the data obtained from the piezoresistive stress sensing cells. The accuracy of measured data is examined by Finite Element method (FEM), and the physical changes are validated with Scanning Acoustic Microscope (SAM).**

***Index Terms*—Stress Sensor, Electronic Control Units, Machine Learning, Fault Detection, Outlier Detection**

I. Introduction

CONDITION Monitoring (CM) is a process to monitor parameters of system conditions, which is a critical component in predictive maintenance. Condition monitoring techniques have been used extensively for large-scale machineries and structures. More recently, condition monitoring has been adopted for advanced electronic systems, most notably, automotive electronics including batteries. Conventional sensors (e.g., sensors for temperature, humidity, vibration, etc.) are not most adequate for the condition monitoring of complex electronic system as they only measure the loading conditions. The piezoresistive stress sensors were developed to cope with the problem. The sensor measures directly the stresses of a silicon chip, and it was utilized in several electronic packaging applications [1] [2] [3] [4] [5] [6] [7] [8] [9]. It was also implemented successfully to monitor the stresses in advanced electronic control unit (ECU) subjected to reliability testing conditions [10] [11]. In order to extend its applicability into the Prognostics and Health Management (PHM) domain, it is required to link the measured stress to the damage or fault of the ECU, as illustrated in Figure 1. Basically, PHM is an algorithm or a set of algorithms based on measurements and models, which collect as an input an already known information about the system/structure and data from strategically positioned sensors. Then it subsequently provides as an output different levels of prognostics such as failure detection, diagnostics and prediction. Various levels of prognostics require different strategies/algorithms for successful implementation.

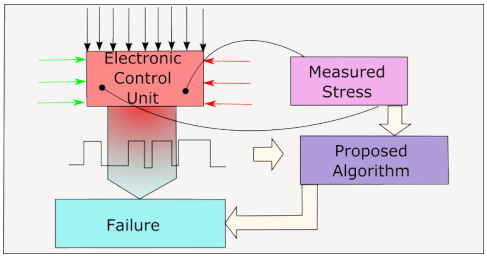

Fig. 1. Stress Failure relationship. Various type of loads are causing ECU failures. The proposed algorithm is linking the measured stress with the failure.

As depicted in Figure 2, a well-implemented prognostic methodology should include the following items:

- Sensors for prognostics
- Data collection, processing, reduction and feature extraction
- Data Security and integrity
- Identification and analyze precursors, Risk and uncertainty analysis
- Health assessment, anomaly detection, fault recognition, fault classification, fault propagation
- Physics-of-Failure (PoF), Damage Models, Reliability testing
- Model Order Reduction, Metamodels, Surrogate Models of Finite Element Methods (FEM) or any other Physical Model

The objective of this paper is to propose special algorithms to handle the stress sensor data obtained from the ECU in order to recognize in-situ failure. To do so The proposed algorithms are presented after briefly describing the sensor. The implementation results are followed using the data obtained from a test vehicle.

II. iForce Sensor

The piezoresistive silicon based stress sensor is constructed of MOSFET transistors in current mirror configuration to

A. Prisacaru, A. Palczynska, P. Gromala are with Automotive Electronics, Robert Bosch GmbH, Reutlingen, Germany (e-mail: Alexandru.Prisacaru@de.bosch.com, e-mail: Alicja.Palczynska@de.bosch.com, e-mail: PrzemyslawJakub.Gromala@de.bosch.com).

A. Theissler is with Automotive Aftermarket, Robert Bosch GmbH, Germany (e-mail: Andreas.Theissler@de.bosch.com).

B. Han is with Mechanical Engineering Department at University of Maryland, College Park MD 20742, USA (e-mail: bthan@umd.edu).

G. Q. Zhang is with Microelectronics Department at Delft University of Technology, Delft, 2600, Netherlands (e-mail: G.Q.Zhang@tudelft.nl).

Fig. 2. Prognostics and Health Management main techniques.

locally measure the stress and the temperature. The measuring principle is based on measuring the resistance which is a function of electrons mobility inside the silicon crystal. A more detailed working principle of the piezoresistive silicon based stress sensor can be found in Refs. [1] and [12]. A land grid array (LGA) package used in this study is shown in Figure 3. It is a standard sensor package, which contains a pair of symmetrically located sensor with 12 sensing cells. Every cell is capable of measuring the in-plane shear stress, σ_{xy}, and the difference of in-plane normal stress components, $D(\sigma) = \sigma_{xx} - \sigma_{yy}$.

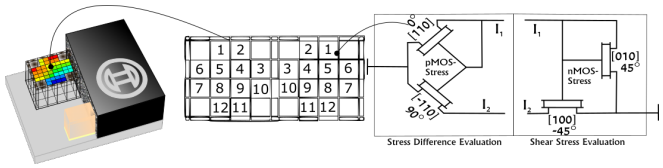

Fig. 3. Sensor cell numbering in a LGA package. P-mos and n-mos MOSFET channels used to acquire the data.

The relationship between the measured currents and the stresses are:

$$\sigma_{xx} - \sigma_{yy} = \frac{1}{\pi_{44}^{p}} \frac{I_{OUT} - I_{IN}}{I_{OUT} + I_{IN}} \tag{1}$$

$$\sigma_{xy} = \frac{1}{\pi_{11}^{n} - \pi_{12}^{n}} \frac{I_{OUT} - I_{IN}}{I_{OUT} + I_{IN}} \tag{2}$$

where π_{11},π_{12},π_{44} are the piezoresistive coefficients of silicon; and I_{IN}, I_{OUT} are the currents measured at the input and output of the sensor, respectively. The stresses can be used to produce the maximum shear stress and the angle of principal stresses as:

$$\tau_{max} = \frac{\sigma_1 - \sigma_2}{2} = \sqrt{\frac{\sigma_{xx} - \sigma_{yy}}{2}^2 + \tau_{xy}^2} \tag{3}$$

$$tan2\theta_p = \frac{2\tau_{xy}}{\sigma_{xx} - \sigma_{yy}} \tag{4}$$

Based on the stress equations a 2D Mohr Circle can be erected and the parameter relationship is depicted in Figure 4. Mohr circle is a graphical representation of all the stress components captured in one circle.

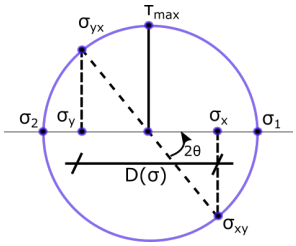

Fig. 4. 2D Mohr Cicle. Describes the relationship between parameters.

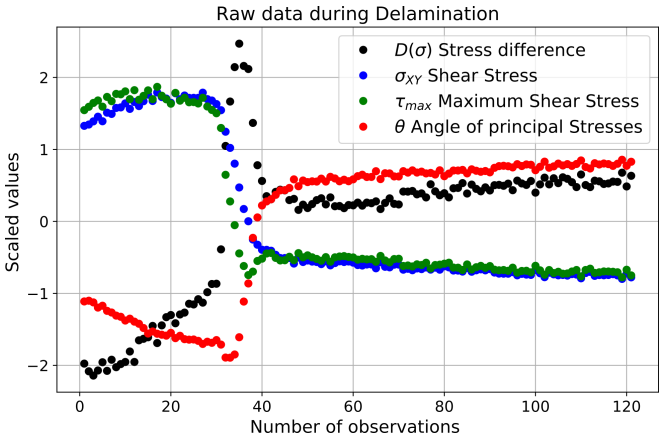

Fig. 5. Raw data example at room temperature during delamination.

The data collected from one cell during failure propagation, represents raw data, two measured parameters and two calculated parameters are shown in Figure 5.

III. Proposed Algorithm

To successfully measure the stresses from the sensors an acquisition unit (AU) is required. The designed AU is able to evaluate the stresses, pre-process the data, extract the features and asses the health as shown in Figure 6. In any case a failure or anomaly is detected then the data is sent to what is called Central PHM ECU unit. The gateway is able to classify the data as being healthy or damaged in which case resilient actions are taken. The workflow of such system is presented bellow.

A typical health dataset, X, contains m rows and p columns, where m is the total number of observations before observing any anomalies and p the total number of the performance parameters. Each sensor output having 12 cells and 4 parameters can have up to 48 performance parameters. The first part of the algorithm starts with extracting and creating an initial healthy baseline, and subsequently assessing the health at every measurement step. If no deviations are detected at that particular data point in time, the healthy baseline is updated as shown in Figure 7.

In this study, Mahalanobis Distance (MD) [10] [13] is employed to assess the health or to detect any anomalies. It is

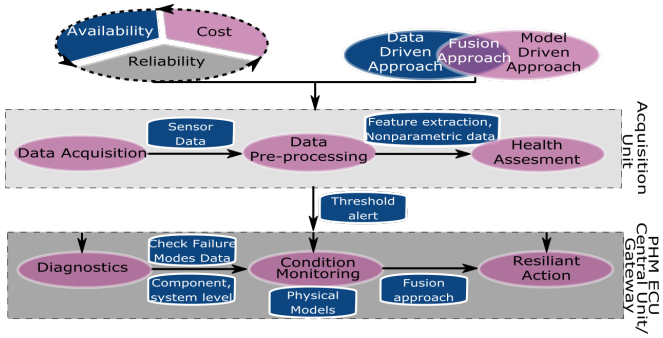

Fig. 6. Prognostics and Health Monitoring framework.

also called quadratic distance as it can measure the difference between two sets of data as well as the distance between a point and a set of data. Although effective, it could detect false signals (e.g., outliers, changes not associated with damage, etc.). An additional step that quantifies the damage is added to avoid false detection. Let us assume that an anomaly is detected at the nth observation. To assure that this detection point is not an outlier, another set of measurement should be conducted at $n + h$, where h depends on the number of performance parameters. A new dataset, Y, is created, containing h rows and p columns. On this newly created dataset h by p, a correlation matrix is constructed. This correlation matrix is assumed to be the failure correlation matrix, and it is compared with the healthy baseline correlation matrix used in MD method. This is possible with Fisher $r - to - z$ transformation [14], which assess the significance of the difference between two correlation coefficients.

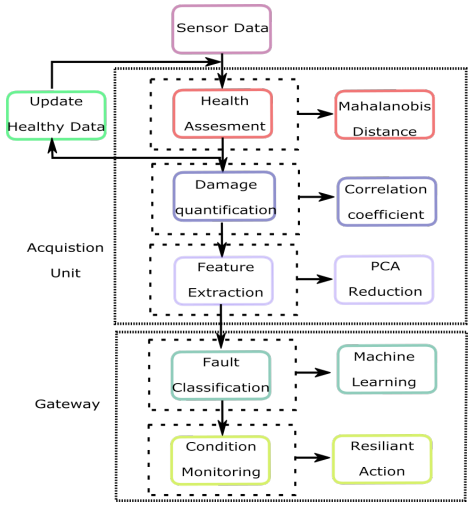

Fig. 7. Algorithm flowchart.

In case that the significance of the difference is close to zero it means that the probability of two sets to be similar is very high. If the z value is around one the probability that these datasets to be similar is less than 0.05. This additional step is checking if the data points are outliers and it can quantify the damage by estimating the $z - scores$ of the performance parameters. As a intermediate step PCA is used for the data reduction to facilitate cheaper and faster transmission [15]. Another main advantage of PCA is that is used to extract features by highlighting the patterns from the data. This step is performed only if MD detects any anomaly and if the significance of the difference between two correlation coefficients is at least equal to one. In this way it is certain that the detection point is not an outlier, but an entire dataset different from the healthy baseline. The extracted features are then use to classify the data by using Support Vector Machines. The data is divided into training and testing datasets in about $70/30\%$ used to validate the classification model.

IV. Implementation

A. Test Vehicle

The test vehicle used in the study is shown in Figure 8 and it represents an Outer molded ECU.

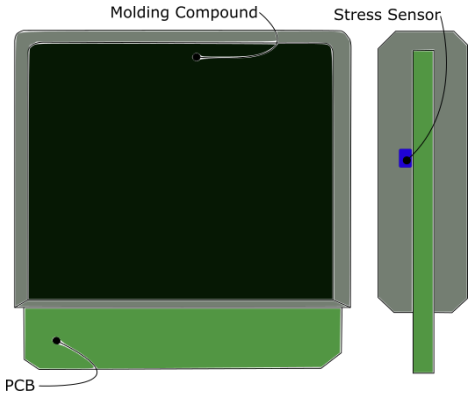

Fig. 8. Geometry representation of the Outer molded electronic control unit.

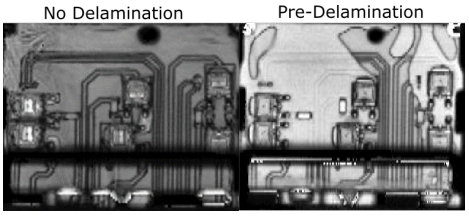

Fig. 9. Process intended pre-delamination.

It consists of six DPAKs and three stress sensors mounted on the top and bottom sides of a PCB as shown in Figure 9. This assembly was molded by an injection molding process. The location of the sensors was chosen to capture the maximum stress. Every sensor package contains 2 symmetrical sensors. Their locations and their arbitrary numbering is presented in Figure 10.

The study was performed on 10 samples, but the results are shown from the most significant 2 samples considering the large amount of data. Some initial delamination was created on the samples before the injection molding process as shown in Figure 9. The delamination areas are visible in the initial SAM images as shown in Figure 11. The locations of delamination are randomly distributed. It is observed that the delamination is present in the vicinity of sensor 3 (S3) in both sides of the PCB of Sample 2. Thus, it is expected that the most damage should be recorded by sensor S3 of Sample 2.

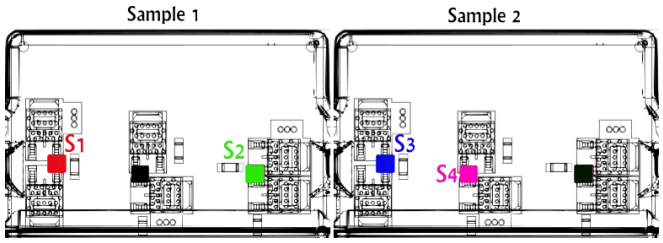

Fig. 10. The position of each sensor on the Outer molded electronic control unit.

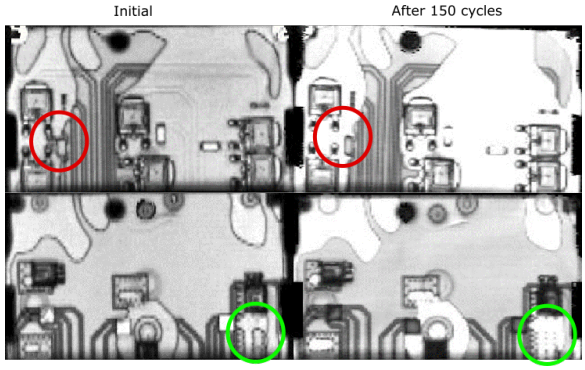

(a) Sample 1. The red and green circles represent the area where there are changes in the delamination.

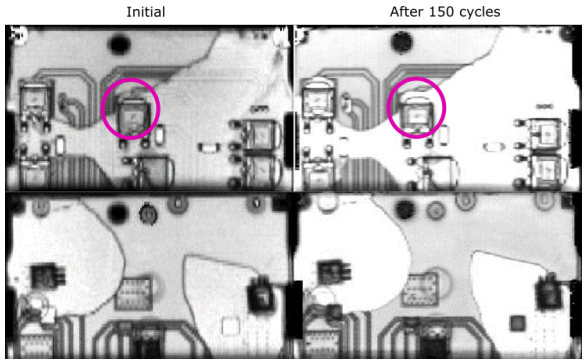

(b) Sample 2. The magenta circles represent the area where there are changes in the delamination area.

Fig. 11. SAM images of the initial delamination and the delamination propagation after 150 cycles.

The delamination is represented by the area in lighter color and the lack of visibility of the circuit board footprint, as shown in Figure 11.

B. Initial Data

Data was recorded through an acquisition system during the experiments. The samples were placed in a temperature chamber, and they were exposed to a passive cycling loading condition of -40 C to 125 C with a dwelling time of 15 minutes. The dwelling time was predetermined to provide a condition where all components reach the uniform distribution at target temperatures. SAM images of the samples were recorded before and after each 150 cycles. The sensor signal was investigated by a predictive FEM model. The geometry and the loading conditions are identical to the experiment as shown in Figure 12. The stress difference and the shear stress

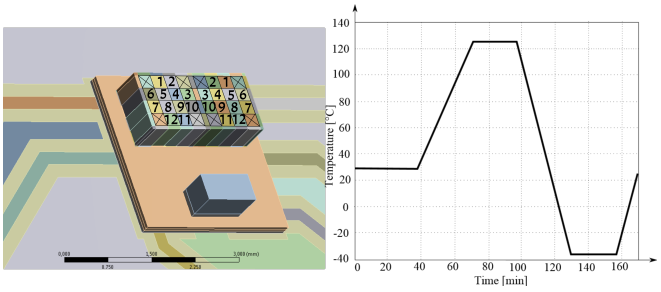

Fig. 12. Stress sensing cells FEM simulation and the loading conditions.

are evaluated at the same location as in the experimental case. The process to validate the model can be found in Ref. [16]. The simulation material models used are linear elastic and linear viscoelastic with their properties shown in Table I.

The modelling predictions are compared with the experimental data in Figure 13. The results show very good agreement. The small deviations are attributed to the uncertainties of the stress sensor [17] and the material properties used in the simulation. The repeatability of measurements is known to be 0.3 MPa, and sample-to-sample variations are $2 - 6$ MPa. From these graphs it is identified the sensitivity of each cell in the healthy stress state. It is clear that from all the parameters, cell 1, 2, 11 and 12 have the highest deviation between different loading conditions. This means that the higher stress state is located at the outer areas of the chip. This observation is important for further development of the stress sensor and also for data reduction strategies. The simulation data is used to examine the measurements. It also provides better understanding about the mechanical processes and ultimately help develop a prognostics physical model. It can be further used for model-based fault detection by considering the residuals, which can be utilized to classify different failure modes behavior.

C. Data from Thermal Cycling Data

Between the first and the 50th cycle, changes in the stress difference and shear stress were observed. Some of these changes are recorded around 50th cycle, and the results are depicted in Figure 9. There are changes in stress difference in both sensors 3a and 3b from Sample 1. The sample and the red circle corresponding to the delamination propagation can be visualized in Figure 7.

Considering Figure from the FEM with healthy data it can be stated that cell 1,2,11 and 12 are the most sensitive cells. All the data and figures are based on the data from one of these cells due to the high sensitivity. From the same interval of cycles it can also be observed a change in difference of stress for sensor 2b from Sample 2 as depicted in Figure 10. The sample and the magenta circle representing the delamination propagation can be visualized in Figure 7. The corresponding shear stress from the interval of cycles described above it can also be observed a change for sensor 3b and 3a from Sample 1 as depicted in Figure 10. The sample and the red circle representing the delamination propagation can be visualized in Figure 7.

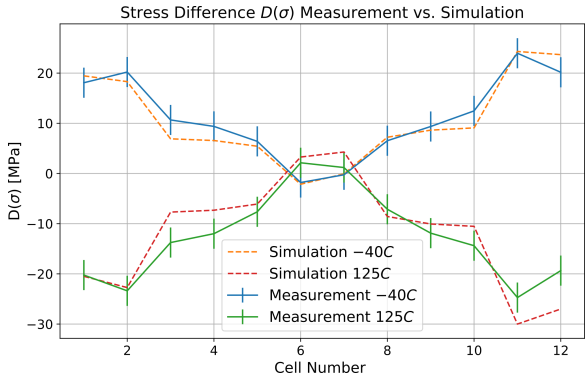

(a) Stress Difference $D(\sigma)$ Measurement vs. Simulation.

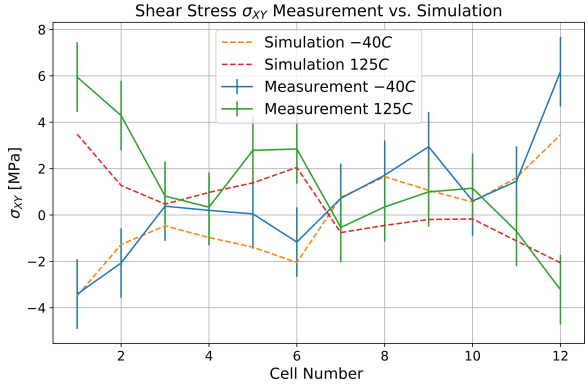

(b) Shear Stress σ_{XY} Measurement vs. Simulation.

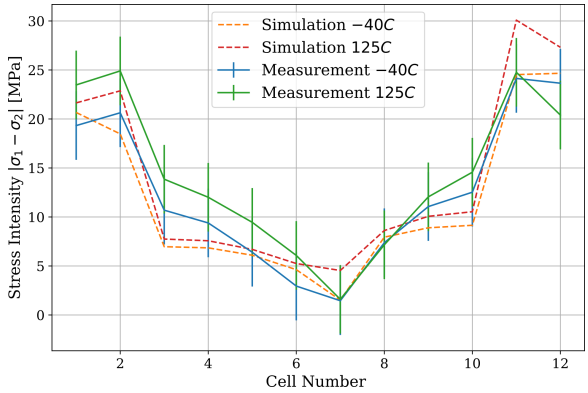

(c) Maximum Shear Stress τ_{max} Measurement vs. Simulation.

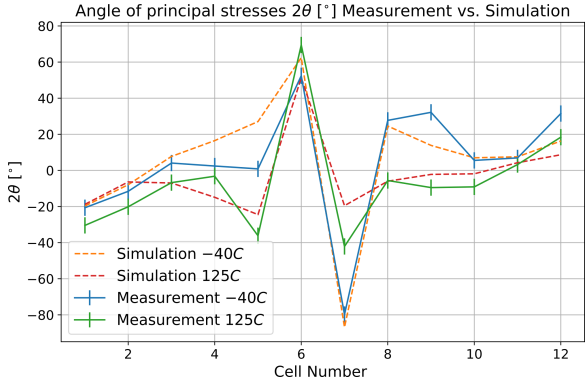

(d) Angle of principal stresses $2\theta[^\circ]$ Measurement vs. Simulation.

Fig. 13. FEM examination of the test vehicle.

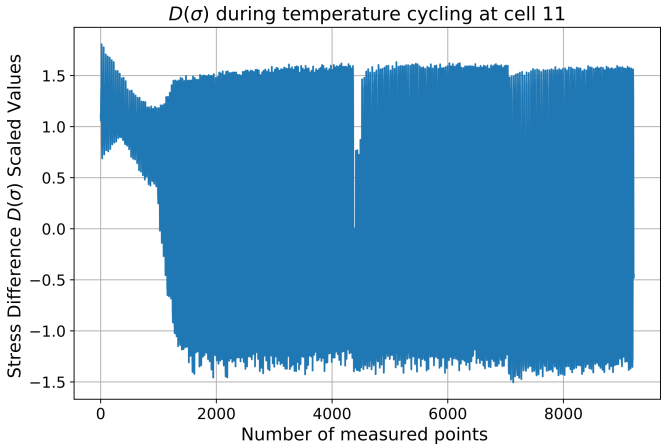

Fig. 14. Stress evolution of the delamination during temperature cycling of the Sample 1 cell 11.

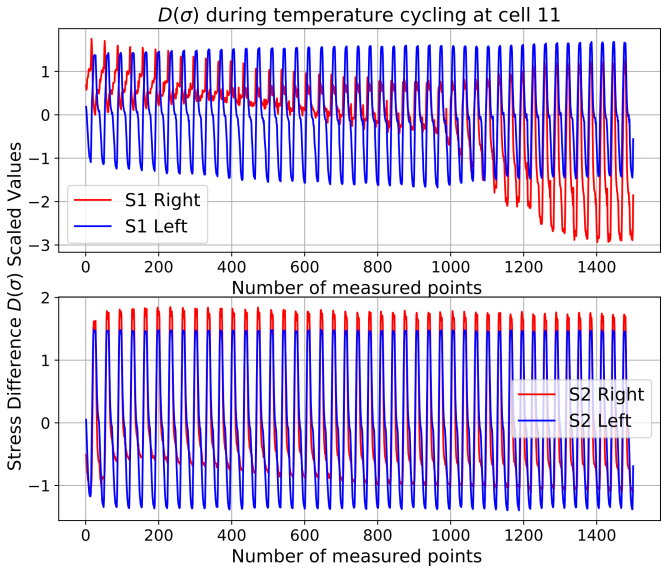

Fig. 15. Stress evolution of the delamination during temperature cycling of the Sample 1.

Due to the complexity of the structure and the big amount of data, it is challenging to interpret the data quantitatively. Several algorithms such as statistical pattern recognition methods and machine learning are considered to interpret the data.

The corresponding shear stress of the Sample 2 is depicted in Figure 12. In the case of Sample 1 there were changes on both components of stress, but in this case there are changes only in the stress difference component.

In order to capture both parameters in one graph, Mohrs circles were plotted during the delamination. The results are shown in Figure 13, where the radius and the diameter represent the maximum shear stress and the difference of the principal stresses, respectively. It is clear from Figure 13 that the diameter increases first and decreases rapidly after approximately 30 cycles. It is speculated that energy release associated with crack propagation may be attributed to the diameter reduction. At low temperatures, the stress state is higher because of the large ΔT from the stress free point temperature. Therefore, any change in stress state can be more

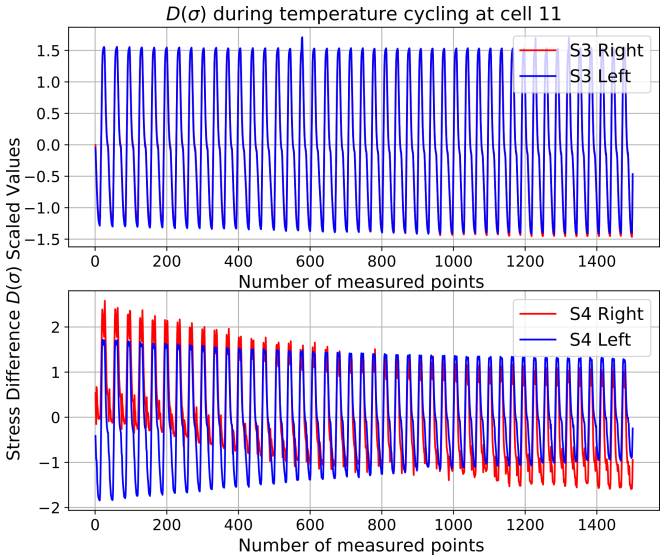

Fig. 16. Stress difference evolution of the delamination during temperature cycling of the Sample 2.

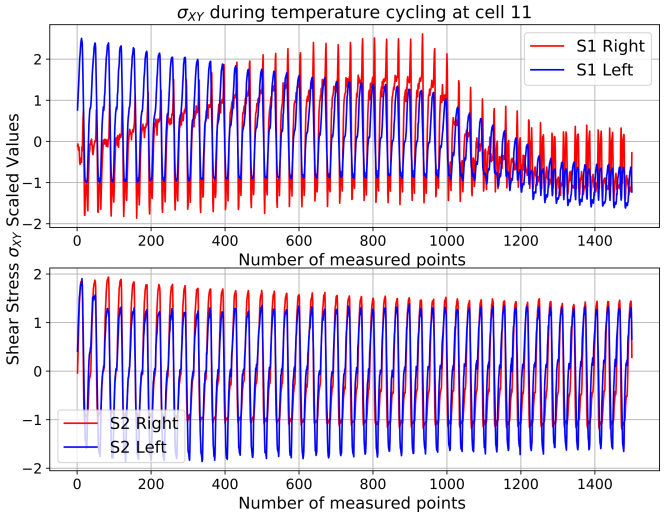

Fig. 17. Shear Stress evolution of the delamination during temperature cycling of the Sample 1.

visible. In addition, the brittle behavior at low temperatures can accelerate the delamination.

D. Failure Analysis by SAM

As shown in Figure 7, changes in the delamination area were observed after 150 cycles. The pictures shown reveals two important properties which should be found in the data as well. The first property is represented by the fact that the samples contain an a priori delamination and the second property by the change in the delamination area due to the damage progress. These properties have correspondence in the data by the stress value differences from the healthy samples and by the ongoing stress change after the cycle 35-50.

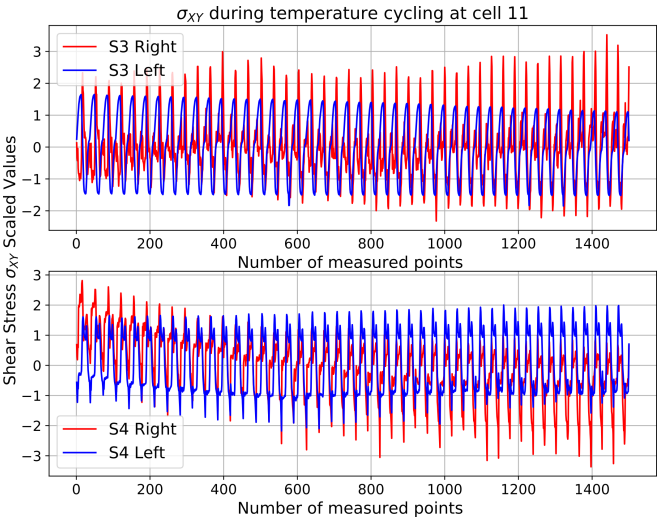

Fig. 18. Shear Stress evolution of the delamination during temperature cycling of the Sample 2.

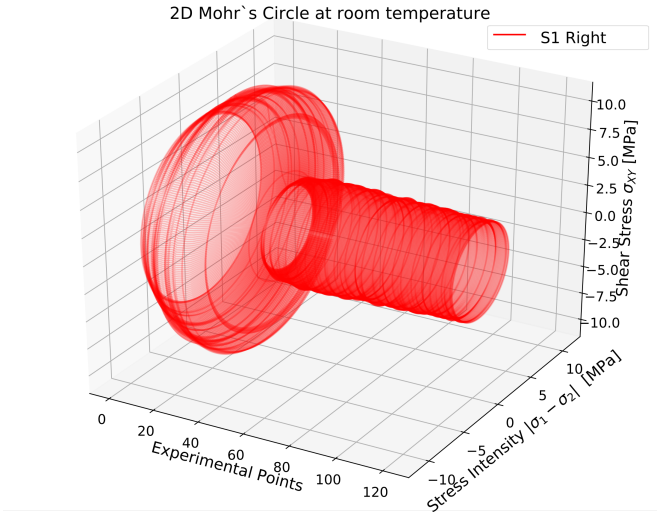

Fig. 19. This is a representation of the 2D Mohr's Circle of the data acquired during the experiments at cell 2 Sample 1 during delamination.

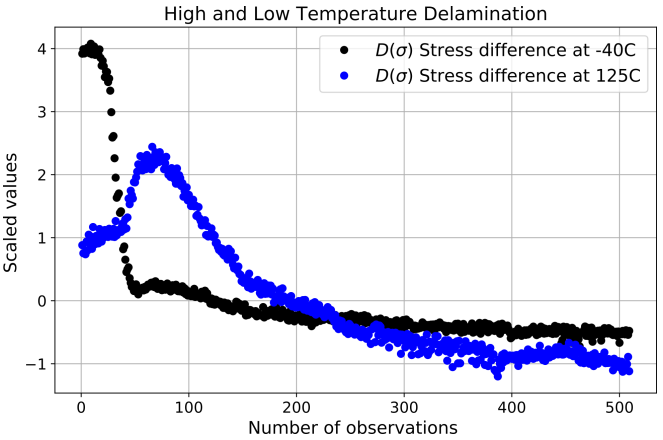

Fig. 20. Stress Difference evolution during delamination at high and low temperature.

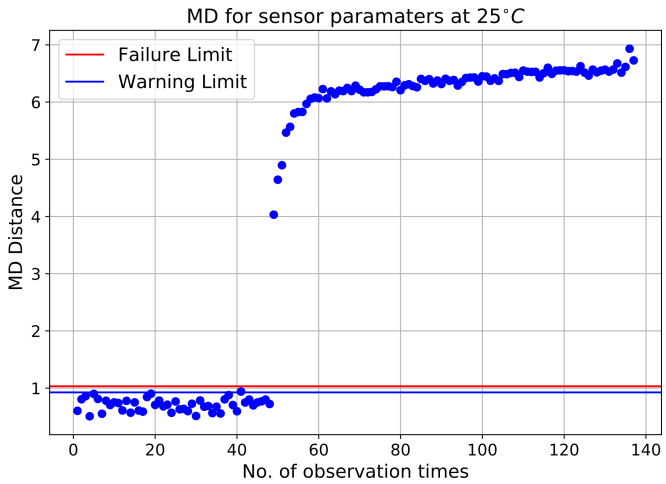

Fig. 21. Mahalanobis Distance calculated over the 12 cells of the Sample 1 S1. The healthy base is established on the first measurements and every point in measurement is calculated. In this graph there is changes due to the delamination showed in Figure 11.

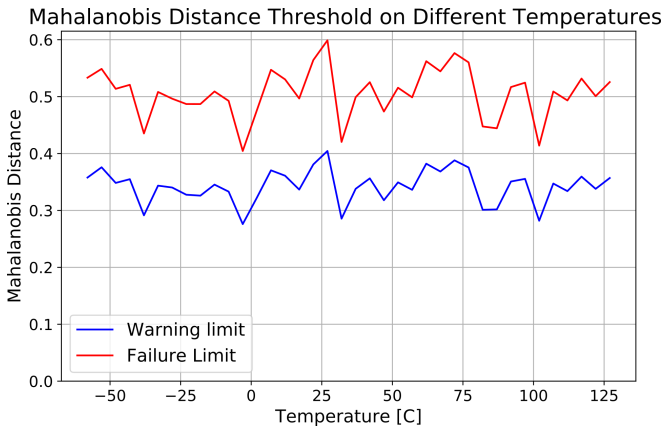

Fig. 22. Threshold Evaluation performed at all temperatures.

V. Data Analysis by the Proposed Algorithm

A. Health Assessment

For computing MD, the sets of compared data do not need to have the same amount of rows. In this study rows refers to the number of observations and creates the possibility to compare the healthy dataset with just one failure measurement point. This is convenient in health monitoring, considering that many other methods require a certain amount of observation points. In this approach a healthy baseline and a threshold are needed to classify the product states (healthy or unhealthy). Several steps are required to calculate MD as follows:

- Step 1. Calculate the average of each column

$$\bar{x_i} = \frac{1}{m}\sum_{j=1}^{m} x_{ij} \tag{5}$$

- Step 2. Calculate the standard deviation

$$S_i = \sqrt{\frac{\sum_{j=1}^{m}(x_{ij} - \bar{x_i})^2}{m-1}} \tag{6}$$

- Step 3. Normalize the values

$$Z_{ij} = \frac{x_{ij} - \bar{x_i}}{S_i} \tag{7}$$

- Step 4. Correlation matrix

$$C = \frac{1}{m-1}\sum_{j=1}^{m} z_j z_j^T \tag{8}$$

- Step 5. Mahalanobis Distance

$$MD_j = \frac{1}{p} z_j^T C^{-1} z_j \tag{9}$$

The next step is to add the normalized values of the next measurement and to compute the MD keeping the same correlation matrix from the healthy baseline. If the measurement point does not exceed the threshold, it is added to the healthy correlation matrix.

For threshold determination, a probabilistic approach is used. Since the MD are not normally distributed, a Box-Cox transformation [18] is used to convert the data into a normal distribution. A warning limit threshold is defined as $(\mu + 2\sigma)$ and a fault alarm threshold as $(\mu + 3\sigma)$, based on the normal distribution parameters. The healthy baseline should have more rows than columns, considering that the rows represents the number of measurements and columns the number of parameters. For assuring good results, it is recommended that the ratio m/p should be as high as possible, otherwise the outliers can shift the sample mean and inflate the correlation matrix [19]. A representative MD for both stress components is shown in Figure 14. The healthy baseline is created on the first 35 measurement points. The data points exceeding the failure limit are clearly seen in the MD results. The incidents are expected from the raw data (Figure 11), but the MD results provide a more definitive health state of the specimen through the multi-variate to uni-variate conversion.

The threshold at different temperatures is computed from the healthy data (i.e., no initial delamination), and the result is plotted in Figure 15. It is evident that the threshold does not change with the temperature, which implies that the healthy baseline can be created at any temperature. MD method is preferred for fault/anomaly detection because of its advantages related to the requirements in health monitoring; they include fast calculation, no failure data requires, single measurement point required and temperature independent threshold.

B. Damage Quantification

This step is necessary to overcome the possibility of detecting outliers or changes in stress values which are not associated with any damage. In this subsection, the correlation matrix of the healthy baseline without initial delamination is compared with the correlation matrix of a potential failure dataset. As previously mentioned, a new correlation matrix is calculated based on the measurement points after the threshold is exceeded.

The sampling distribution of the healthy and faulty correlation coefficient matrices does not follow a normal distribution. Fisher r-to-z transformation is used to convert these data sets

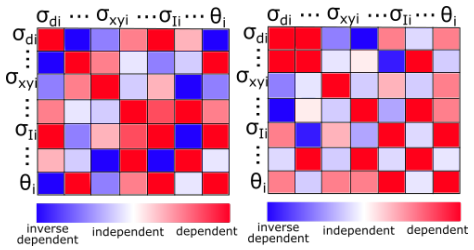

Fig. 23. Healthy baseline Correlation Matrix vs. Outlier baseline Correlation Matrix.

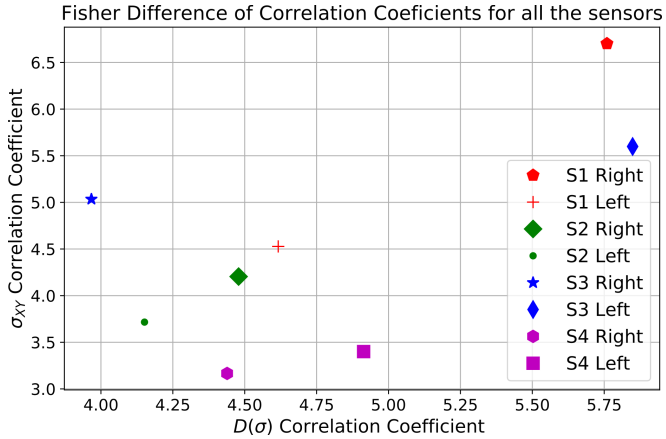

Fig. 24. Fisher Correlation Coefficient Difference. This difference is performed by using Fisher method of comparing two correlation coefficients. In this case all the sensors correlation coefficient data have been compared with the correlation coefficient as healthy state. The values from the graph represents the z-score values.

into a normally distributed variable z. This transformation is made as follows:

$$z_r = \frac{1}{2} log(\frac{1+r}{1-r}) \tag{10}$$

This transformation is performed at a confidence value interval of 0.95. Each correlation coefficient parameter in the data is compared with the correspondent one and then a mean is performed on the stress difference and shear stress performance parameters. Plotting them against each other is depicted in Figure 16. From this graph it is concluded that some sensor data is more damaged than the others. The most damaged one is showed in yellow representing the Sample 3 sensor 3a. From Figure 7 it is observed that the outer molding compound is delaminated from the package of sensor 3a.

C. Feature Extraction

PCA is used to identify patterns in data of high dimension and to express the data to highlight their similarities and differences [15]. Also, this last step is performed to reduce the data as much as possible, to understand the data much better and to make the classification much easier to be performed.

Another main advantage of PCA is finding the patterns in data by reducing the number of dimensions without much loss of information. This technique is very useful in case of linking the stress sensor data to the failure.

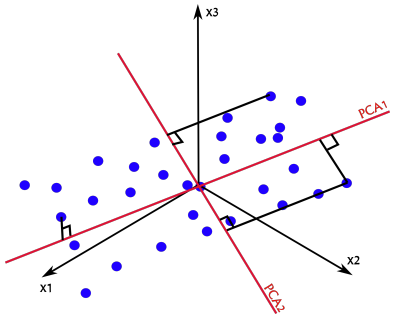

Fig. 25. Visual representation of the reduced space.

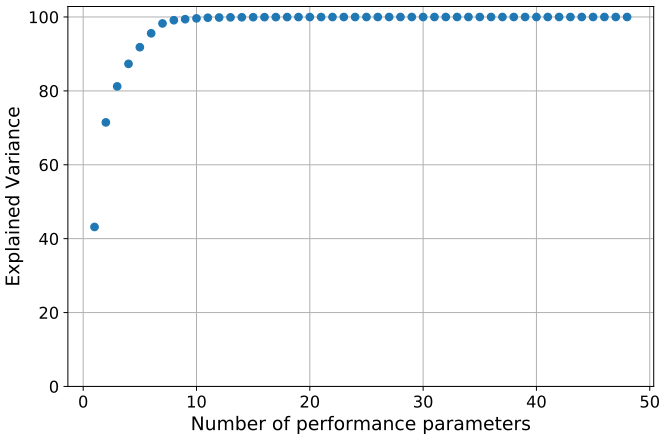

Fig. 26. Explained variance.

The PCA analysis is performed on the data matrix and the explained variance is extract as shown in Figure 17. Only the principal components exceeding 97% of the variance are kept. Therefore only 6 principal components are left to perform PCA analysis and the extracted results of each performance parameter influence on the principal components is shown in TABLE I. It is observed that the weight of each parameter reveals that the first component takes the most influence from stress difference performance parameters and the second component takes the effect from shear stress performance parameters. Plotting first and second component as in Figure 18 it is observed the influence of stress difference and shear stress in the delamination process. Again as previously observed, the yellow markers representing sensor 3 from Sample 2 is situated as the most damaged one. The sensor symmetry is identified from Figure 18 and Figure 19. The behavior of the sensors in both figures is quite similar, but with opposite sign. Considering this property, a classification strategy can be implemented, considering the data from one sensor as training data and the data from the other sensor as validation. Briefly a PCA is performed as follows:

- Step 1. Subtract the mean

$$\bar{x_i} = \frac{1}{m} \sum_{j=1}^{m} x_{ij} \tag{11}$$

- Step 2. Calculate the covariance matrix

$$cov(x_i, x_j) = \frac{\sum_{i,j}^{n} (x_i - \bar{x})(x_j - \bar{x})}{n-1} \tag{12}$$

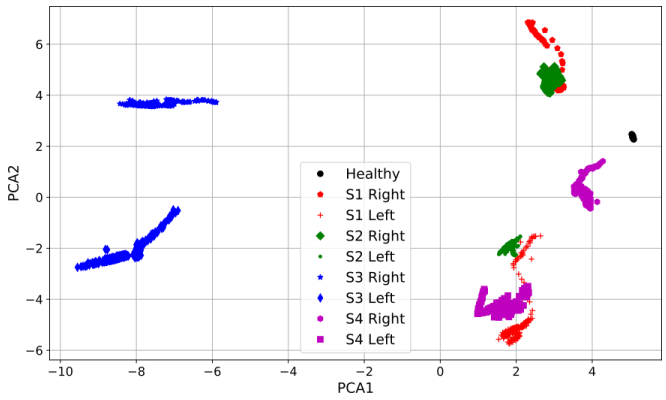

Fig. 27. Principal components influence over the delamination areas.

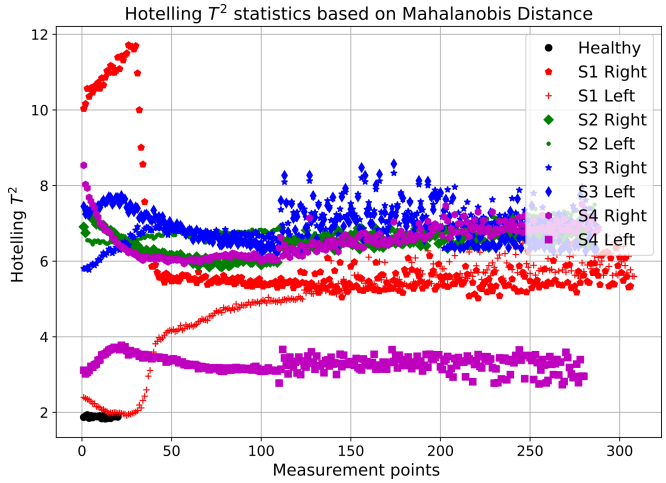

Fig. 28. Hoteling T2 statistics in the reduced space at room temperature during delamination. The red line corresponding to the same sensor but mirrored can identify a similar behavior, but opposite sign.

- Step 3. Calculate the eigenvectors and eigenvalues of the covariance matrix
- Step 4. Choosing the eigenvectors with the highest eigenvalue
- Step 5. Reconstructing the data matrix with the new set of parameters

With the data reduced to 6 performance parameters, it can be furthered used for transmitting the data. The transmitted data can be reconstructed in the initial number of parameters or it can be used as it is. The classification methods can use both datasets.

In Figure 18 the most dominant principal components are depicted, reducing the high dimension of the data to these 2 components makes it easier to understand the global influence of different delamination areas on the stress difference and shear stress components. As expected the sensor 3a and 3b data from Sample 2 shows the biggest distance from the healthy baseline at least in the first component axis, which is represented in most part by stress difference component.

Based on the reduced space Hoteling T2 statistics is performed and is depicted in Figure 19. In this graph is observed as well that the stresses reach a high peak and then there is a drop, which confirms our previous observations that before the

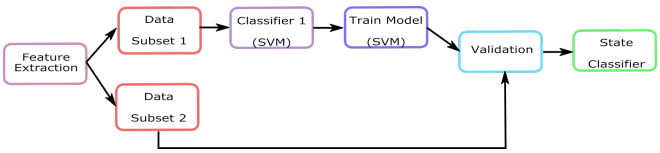

Fig. 29. Classification Method.

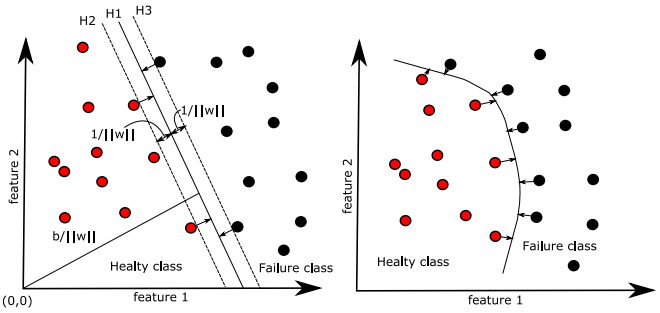

Fig. 30. Support Vector Machine; linear and nonlinear boundary.

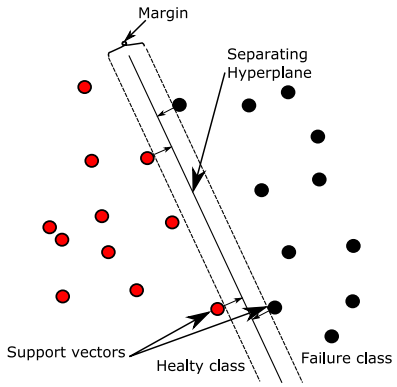

Fig. 31. Classification linear case.

delamination there is an increase in the stress state followed by a drop representing the physical delamination.

D. Fault Classification

1) Support Vector Machines: Support Vector Machines(SVM) are a set of supervised machine learning method that can be applied to structural damage detection due to their ability to form an accurate boundary from a small amount of training data [18]. In fact SVM is a technique of finding the plane separating the two datasets and to maximize the distance between them for the classification purpose. During the training the algorithms finds the best hyperplane between sets of data in the feature space. The best hyperplane is the one that maximizes the distances between classes. A hyperplane can be linear or nonlinear boundary.

One example of linear and nonlinear boundary hyperplane is depicted in Figure 30. When a linear separator cannot be created, data points are projected into an higher-dimensional space where the data points become linearly separable (the projection is performed with kernel techniques).

The classification in linear case is performed by considering plane $H1$ written as $wx + b = 0$, where w is normal to

the hyperplane, x the points which lie on the hyperplane. All training data must satisfy the following constraints:

$$x_i w + b \geq +1 \quad for \quad y_i = +1 \tag{13}$$

$$x_i w + b \leq -1 \quad for \quad y_i = -1 \tag{14}$$

All these being combined into one set of inequalities:

$$y_i(x_i w + b) - 1 \geq 0 \tag{15}$$

The points for which the equality 13 holds, lay on the hyperplane $H2$ and respectively the points for which the equality 14 hold they are laying on the hyperplane $H3$. Hence the distance between $H1$ and $H2$ is $d_+ = 1/||w||$ and the margin is simply $2/||w||$. Considering that $H2$ and $H3$ are parallel and no points lies between them, the optimization problem needs to minimize $||w||^2$, which is subjected to constraints.

The solution to this problem for a typical two dimensional case looks like in Figure 31. The optimization problem it is solved by Lagrangian multipliers by changing the contraints into Lagrangian multipliers. The objective function can be written as:

$$L_p = \frac{1}{2}||w||^2 - \sum_{i=1}^{l} \alpha_i y_i (x_i w + b) + \sum_{i=1}^{l} \alpha_i, \tag{16}$$

where α_i are positive Lagrangian multipliers. The aim is to minimize L_p with respect to w and b. The non-linear classification involves mapping the data points from a lower dimensional feature space into a higher dimensional space. This can be made by a function which is called a kernel function. There are several functions used in the literature, but the ones used in this study are :

$$K(x_i, x_j) = \begin{cases} x_i \cdot xj \quad Linear \\ (\gamma x_i \cdot x_j + C)^d \quad Polynomial \\ \exp(-\gamma |x_i - x_j|^2) \quad RBF \end{cases} \tag{17}$$

Fortunate in this case of using successfully PCA to reduce and to extract feature data, classification is not a big challenge and even a linear kernel can do the work.

VI. Conclusion

It has been demonstrated that the piezoresistive silicon based stress sensor is capable of detecting and quantifying delamination. Also, the resulting data shows the symmetry of the sensors. The algorithms applied to the sensor data revealed valuable information that can be furthered studied. Further research studies will be performed on the importance of the new parameters and their connection to the failure, the slope registered at the temperature cycling during delamination, classification methods applied to principal components and the possibility to build a prognostic model based on the damage quantification parameter. The ultimate goal is to develop and implement PHM for various application requirements. Usually these requirements are projected into a PHM Framework. There are many PHM frameworks proposed in the literature for different applications [18][20]. The principles are in general the same for most of them, but for each particular application PHM frameworks must be modified and optimized for specific requirements. In the present case of ECU application, it is desired to have certain calculations and data processing inside the acquisition system as depicted in Figure 20. In this paper the first part of this framework was presented, which is the data acquisition, data manipulation, health assessment and damage quantification. The second part of the frame work will be reported in the future publication.

Appendix A
Table Section

Appendix B

Acknowledgment

The authors would like to thank...

References

[1] J. C. Suhling, R. C. Jaeger, and others, "Silicon piezoresistive stress sensors and their application in electronic packaging," vol. 1, no. 1, pp. 14–30. [Online]. Available: http://js-engineering.com/Assets/SensorsJournal01.pdf

[2] P. Gromala, S. Fischer, T. Zoller, A. Andreescu, J. Duerr, M. Rapp, and J. Wilde, "Internal stress state measurements of the large molded electronic control units," in *Thermal, Mechanical and Multi-Physics Simulation and Experiments in Microelectronics and Microsystems (EuroSimE), 2013 14th International Conference on*. IEEE, pp. 1–8. [Online]. Available: http://ieeexplore.ieee.org/abstract/document/6529894/

[3] T. Schreier-Alt, K. Unterhofer, F. Ansorge, and K.-D. Lang, "Stress analysis during assembly and packaging," in *Electronic Components and Technology Conference (ECTC), 2011 IEEE 61st*. IEEE, pp. 1684–1690. [Online]. Available: http://ieeexplore.ieee.org/abstract/document/5898738/

[4] A. R. Adli and K. Jansen, "Numerical investigation and experimental validation of residual stresses building up in microelectronics packaging," vol. 62, pp. 26–38. [Online]. Available: http://linkinghub.elsevier.com/retrieve/pii/S0026271416300506

[5] T. Schreier-Alt, G. Chmiel, F. Ansorge, and K.-D. Lang, "Piezoresistive stress sensor for inline monitoring during assembly and packaging of QFN," in *Electronic Components and Technology Conference (ECTC), 2013 IEEE 63rd*. IEEE, pp. 2126–2131. [Online]. Available: http://ieeexplore.ieee.org/abstract/document/6575874/

[6] F. Schindler-Saefkow, F. Rost, A. Rezaie-Adli, K. M. B. Jansen, B. Wunderle, J. Keller, S. Rzepka, and B. Michel, "Measuring the mechanical relevant shrinkage during in-mold and post-mold cure with the stress chip," in *Thermal, mechanical and multi-physics simulation and experiments in microelectronics and microsystems (eurosime), 2014 15th international conference on*. IEEE, pp. 1–5. [Online]. Available: http://ieeexplore.ieee.org/abstract/document/6813807/

[7] Y. Kim, H. Lee, S. Park, and X. Zhang, "Stress relaxation test of molding compound for MEMS packaging," in *Thermal and Thermomechanical Phenomena in Electronic Systems (ITherm), 2012 13th IEEE Intersociety Conference on*. IEEE, pp. 290–296. [Online]. Available: http://ieeexplore.ieee.org/abstract/document/6231442/

[8] A. Palczynska, P. J. Gromala, D. Mayer, B. Han, and T. Melz, "In-situ investigation of EMC relaxation behavior using piezoresistive stress sensor," vol. 62, pp. 58–62. [Online]. Available: http://www.sciencedirect.com/science/article/pii/S0026271416300488

[9] M. K. Rahim, J. Roberts, J. C. Suhling, R. C. Jaeger, and P. Lall, "MEASUREMENT OF DIE STRESSES DURING THERMAL CYCLING."

[10] A. Palczynska, A. Prisacaru, P. J. Gromala, B. Han, D. Mayer, and T. Melz, "Towards prognostics and health monitoring: The potential of fault detection by piezoresistive silicon stress sensor," in *Thermal, Mechanical and Multi-Physics Simulation and Experiments in Microelectronics and Microsystems (EuroSimE), 2016 17th International Conference on*. IEEE, pp. 1–8. [Online]. Available: http://ieeexplore.ieee.org/abstract/document/7463344/

TABLE I
MATERIAL PROPERTIES.

Component	Conductivity $[W/mK]$	Young's Modulus $[MPa]$	Poisson's ratio	CTE below T_g $[1/K]$	CTE above T_g $[1/K]$	T_g $[^\circ C]$	Heat capacity [J/kgK]	Type
Outer Mold	1.00	17000	below T_g : 0.35 above T_g : 0.35	12.00E-6	25.0E-6	110	9.3E8	LVE LVE
PCB copper	350	125000	0.343	1.7E-05	-	-	3.58E+08	Elastic
Lead Frame	350	75000	0.343	1.7E-05	-	-	3.58E+08	Elastic
PCB prepreg	0.7	24706.52	below T_g : 0.35 above T_g : 0.45	X:14E-06 Y:16E-06 Z:52E-06	X:40E-06 Y:40E-06 Z:247E-06	149	8.98E+08	LVE
DPAK mold	1.62	16600	below T_g : 0.25 above T_g : 0.45	1.2E-05	4E-05	100	1.4E+09	LVE
Sensor Mold	0.75	25700	below T_g : 0.35 above T_g : 0.45	8.2E-06	2.67E-05	106	1.4E+09	LVE
Stress Sensor	120	Ex:168.9E+03 Ey:168.9E+03 Ez:130.2E+03	ν_{xz} : 0.361 ν_{xy} : 0.361 ν_{yz} : 0.064	2.8E-06	-	-	7.7E+08	Elastic
Al bond	230	64000	0.33	2.53E-05	-	-	9.1E+08	Elastic
Solder	33	49551	0.36	ALPX	-	-	2.38E+08	Elastic
Die attach	1	7632	below T_g : 0.35 above T_g : 0.45	5.10E-05	1.71E-04	37.55	9.87E+08	LVE
Bt core	-	161171.3	0.35	ALPX	-	110	-	LVE
Ceramic	350	107000	0.25	5E-06	-	-	3.85E+08	Elastic

TABLE II
PCA REDUCED SPACE PARAMETERS

	1	2	3	4	5	6
D(σ)	**0.203**	0.032	0.039	0.085	-0.045	-0.203
	0.209	-0.019	-0.086	0.070	-0.064	-0.065
	0.174	-0.110	-0.160	0.001	0.057	0.163
	0.213	-0.010	-0.093	0.029	-0.039	0.026
	0.213	0.051	0.014	-0.021	-0.016	-0.049
	0.189	0.092	0.136	-0.094	-0.036	-0.090
	0.173	0.125	0.154	-0.130	0.038	-0.034
	0.209	0.059	0.061	-0.083	0.008	0.009
	0.212	-0.039	-0.031	0.072	-0.004	0.087
	0.191	-0.090	-0.074	-0.009	0.030	0.220
	0.208	-0.037	-0.066	-0.050	0.011	0.097
	0.200	0.065	0.079	-0.107	0.049	0.058
σ_{XY}	-0.039	**0.247**	0.128	-0.107	0.054	0.088
	-0.031	**0.257**	0.102	0.041	0.023	-0.088
	-0.009	**0.259**	0.085	0.095	-0.006	-0.039
	-0.039	**0.245**	0.117	-0.027	0.145	-0.127
	-0.021	**0.257**	0.123	0.003	-0.053	0.089
	-0.022	**0.256**	0.019	-0.162	-0.039	0.054
	0.069	**0.179**	0.110	0.270	-0.230	0.164
	-0.043	**0.249**	-0.134	0.013	0.015	0.045
	-0.006	**0.252**	-0.080	-0.150	0.084	0.014
	-0.117	**0.198**	-0.180	-0.003	0.087	-0.001
	-0.153	**0.008**	-0.203	0.183	0.255	-0.111
	0.043	**0.154**	-0.319	-0.096	0.066	-0.139

[11] B. Wu, D.-S. Kim, B. Han, A. Palczynska, and P. J. Gromala, "Thermal deformation analysis of automotive electronic control units subjected to passive and active thermal conditions," in *Thermal, Mechanical and Multi-Physics Simulation and Experiments in Microelectronics and Microsystems (EuroSimE), 2015 16th International Conference on*. IEEE, pp. 1–6. [Online]. Available: http://ieeexplore.ieee.org/abstract/document/7103085/

[12] A. Palczynska, F. Pesth, P. J. Gromala, T. Melz, and D. Mayer, "Acquisition unit for in-situ stress measurements in smart electronic systems," in *Thermal, mechanical and multi-physics simulation and experiments in microelectronics and microsystems (eurosime), 2014 15th international conference on*. IEEE, pp. 1–4. [Online]. Available: http://ieeexplore.ieee.org/abstract/document/6813795/

[13] S. Kumar, V. Sotiris, and M. Pecht, "Health assessment of electronic products using mahalanobis distance and projection pursuit analysis," vol. 2, no. 4, pp. 242–250. [Online]. Available: http://www.waset.org/publications/8544

[14] R. A. Fisher, "Biological monographs and manuals vol-5." [Online]. Available: http://krishikosh.egranth.ac.in/handle/1/2028664

[15] H. Anton, *Elementary linear algebra*. Wiley, OCLC: 13580207.

[16] D.-S. Kim, B. Han, A. Yadur, and P. J. Gromala, "Electronic control package model calibration using moir interferometry," in *Thermal, mechanical and multi-physics simulation and experiments in microelectronics and microsystems (eurosime), 2014 15th international conference on*. IEEE, pp. 1–5. [Online]. Available: http://ieeexplore.ieee.org/abstract/document/6813835/

[17] A. Palczynska, F. Schindler-Saefkow, P. Gromala, K. Kreyig, S. Rzepka, D. Mayer, and T. Melz, "Investigation of uncertainty sources of piezoresistive silicon based stress sensor," vol. 807, pp. 45–54. [Online]. Available: http://www.scientific.net/AMM.807.45

[18] C. J. Burges, *A Tutorial on Support Vector Machines for Pattern Recognition*, 2nd ed. Data Mining and Knowledge Discovery, 1998, vol. pp. 121-167.